Letters

IOP Publishing | Nanotechnology

Nanotechnology **27** (2016) 31LT02 (7pp) | doi:10.1088/0957-4484/27/31/31LT02

Letter

Near-theoretical fracture strengths in native and oxidized silicon nanowires

Frank W DelRio[1], Ryan M White[1], Sergiy Krylyuk[2], Albert V Davydov[2], Lawrence H Friedman[2] and Robert F Cook[2]

[1] Material Measurement Laboratory, National Institute of Standards and Technology, Boulder, CO 80305, USA

[2] Material Measurement Laboratory, National Institute of Standards and Technology, Gaithersburg, MD 20899, USA

E-mail: frank.delrio@nist.gov

Received 8 April 2016, revised 1 June 2016
Accepted for publication 1 June 2016
Published 21 June 2016

Abstract

In this letter, fracture strengths σ_f of native and oxidized silicon nanowires (SiNWs) were determined via atomic force microscopy bending experiments and nonlinear finite element analysis. In the native SiNWs, σ_f in the Si was comparable to the theoretical strength of Si$\langle 111 \rangle$, $\approx$22 GPa. In the oxidized SiNWs, σ_f in the SiO_2 was comparable to the theoretical strength of SiO_2, $\approx$6 to 12 GPa. The results indicate a change in the failure mechanism between native SiNWs, in which fracture originated via inter-atomic bond breaking or atomic-scale defects in the Si, and oxidized SiNWs, in which fracture initiated from surface roughness or nano-scale defects in the SiO_2.

Keywords: fracture strength, silicon nanowires, atomic force microscopy, rapid thermal oxidation, reliability

(Some figures may appear in colour only in the online journal)

1. Introduction

Silicon nanowires (SiNWs) have recently attracted significant attention in a number of various application areas, in large part due to their unique mechanical [1], electrical [2], optical [3], piezoelectrical [4], and thermoelectrical [5] properties. To take advantage of these properties in commercially-viable SiNW-based devices, the structural or load-bearing reliability of SiNWs over the intended device lifetimes is critical. Such reliability depends on the fracture strength of the SiNWs, which, in turn, depends greatly on phenomena that are significant only at the nanoscale SiNW dimensions. The fracture strength σ_f of SiNWs has been shown to approach the theoretical strength of Si [6], which is 17 to 26 GPa depending on the crystallographic orientation [7]. This σ_f range is only possible with critical flaw sizes on the order of a few nm [8], indicating that the strength of native SiNWs is dictated by *intrinsic* planar defects in the Si such as stacking faults or twin boundaries. Strength control by such volume defects is only possible in SiNWs that have surfaces with small areas or near-ideal structures. Furthermore, it has been demonstrated that σ_f values for SiNWs can drop precipitously from the theoretical levels through the development of larger, *extrinsic* flaws due to changes in: (1) surface area or (2) processing conditions [8]. On point (1), there have been several reports on the dependence of σ_f on surface area A_s [9–11], with all in agreement that σ_f decreases as A_s increases. The mechanism behind the trend is well-defined: a given processing method produces a particular distribution of defect sizes, and the probability of a component containing a larger defect increases with A_s, a phenomenon often described by Weibull size-scaling analyses [12]. On point (2), there have been far fewer reports, although most notably the effects of oxidation on σ_f have been considered. In one study, the authors assessed σ_f for both as-grown and fully-oxidized SiNWs, and showed that σ_f decreased by a factor of three on oxidation [13].

 © 2016 IOP Publishing Ltd Printed in the UK

However, the investigation lacked σ_f data for partially-oxidized SiNWs, and was therefore unable to comment on the intermediate trends or the mechanism behind the reduction. Moreover, the strength calculations neglected nonlinear elastic effects, despite the large deformations in the SiNWs.

In this letter, σ_f of native and partially-oxidized SiNWs were measured using atomic force microscopy (AFM) bending experiments. Rapid thermal oxidation (RTO) was performed at 1000 °C for times t of 0 to 30 min to form SiO_2 layers on the SiNWs. Dispersed SiNWs were supported on Si(100) substrates and bent by AFM manipulation until fracture occurred. Nonlinear finite element analysis (FEA) was used to convert curvature at fracture κ_f to σ_f. As t increased, the AFM-based bending tests showed that σ_f decreased from 22 to 12 GPa. More importantly, it was found that the decrease in σ_f was non-monotonic. Instead, σ_f decreased significantly at small t and gradually increased at large t, consistent with the idea that σ_f is initially dictated by inter-atomic bond breaking or atomic-scale defects in the Si but later defined by roughness or nano-scale defects in the SiO_2.

2. Materials and methods

SiNW growth from the vapor-liquid-solid (VLS) process was catalyzed with commercially-available 60 nm Au nanoparticles randomly dispersed on poly-L-lysine-functionalized Si(111) substrates. Growth was performed at 900 °C and 80 kPa (600 Torr) using 30 sccm (standard $cm^3 min^{-1}$) of $SiCl_4$ and 200 sccm of H_2 diluted with N_2 to a total flow rate of 1000 sccm. The Au droplets on the SiNW tips were removed with the following process: (1) etched in a 1:10 HF: deionized (DI) water solution for 10 s, (2) rinsed in DI water, (3) etched in an aqueous $KI:I_2$ solution for 5 min, (4) rinsed in DI water, and (5) dried in an N_2 flow. RTO of SiNWs was performed at 1000 °C for t from 0.5 to 30 min using a 1:10 O_2:Ar mixture [14]. SiNWs were released via ultrasonic agitation in isopropyl alcohol and the solution was deposited on grids and Si(100) substrates to assess the oxidation kinetics and fracture properties, respectively.

SiNW length and cross-section were investigated via scanning electron microscopy (SEM) and transmission electron microscopy (TEM), respectively. SEM was conducted with an accelerating voltage of 20 kV at a 30° tilt. TEM was executed at an accelerating voltage of 200 kV, with the SiNWs tilted to a two beam condition and the images created with a diffraction vector $\boldsymbol{g} = \langle 111 \rangle$. SiNW oxidation kinetics were assessed via annular dark field (ADF) scanning transmission electron microscopy (STEM) images at an accelerating voltage of 200 kV and inner and outer collection angles of 90 mrad and 370 mrad, respectively. For STEM, the SiNWs were tilted to the Si [110] zone axis and focused such that the Si dumbells characteristic of the [110] zone axis were clearly visible. During the SiO_2 layer thickness measurements, the SiO_2 was distinguished from the Si based on the ADF intensity difference. The cross-sectional shapes of the SiNWs were determined by first calculating the dimensions of a base as-fabricated hexagonal SiNW with SiO_2 thickness $t_{ox} = 0$ nm using the STEM measurements of the native SiNW and the molar volumes of Si and SiO_2. The exterior (angular) cross sections of the oxidized SiNWs were attained using the nanowire radius R_{NW} and t_{ox} values from the STEM images and linear interpolation between the (radial) dimensions of the as-fabricated SiNW and the $t = 30$ min SiNW of assumed cylindrical section. The interiors of the cross-sections were determined by radial scaling of the exterior cross-sections from the STEM data. The facet radii and relative Si and SiO_2 volumes were assessed by fitting circles to, and numerical integration of, the interpolated profiles, respectively.

SiNW fracture properties were determined via AFM bending tests using probes with single-crystal Si cantilevers and integrated tips (tip radius $R_t \approx 20$ nm, spring constant $k_c \approx 48$ N m^{-1}). Detailed descriptions of the AFM bending protocol can be found in previous work [6, 13]. In short, the AFM bending tests alternated between topography images and manipulation steps. Initially, each SiNW was straight, and a hook was created at one end by dragging the AFM tip along the Si(100) substrate and moving the SiNW in a prescribed direction. After a hook was created, the curvature κ was increased by moving the shorter end towards the longer end. The manipulation displacements spanned from 1 μm down to 50 nm, with the size decreasing as the number of manipulation steps increased to allow for better resolution of κ_f. To determine κ_f, the SiNW neutral axis just prior to fracture was traced [15] and the x and y coordinates from this process were utilized to calculate κ via $\kappa = |d^2y/dx^2|/(1 + [dy/dx]^2)^{3/2}$.

FEA simulations of the bent SiNWs were utilized to convert κ_f to σ_f and account for two main phenomena: (1) changes in the SiNW cross-section with t and (2) nonlinear effects associated with large κ. In detail, FEA was used to model the mechanical deformation in a thin slice of each SiNW via quadratic wedge-shaped elements [16]. A relative rotation was applied to each cross-section to find the maximum longitudinal Cauchy stress σ_{max} versus κ. Geometrical and material symmetry were consistent with zero-warping assumptions. Constitutive material behavior was modeled as nonlinear hyperelastic with the energy versus Green strain formulation: $U = \frac{1}{2}c_{ij}\varepsilon_i^G\varepsilon_j^G + \frac{1}{6}c_{ijk}\varepsilon_i^G\varepsilon_j^G\varepsilon_k^G + \frac{1}{24}c_{ijkl}\varepsilon_i^G\varepsilon_j^G\varepsilon_k^G\varepsilon_l^G + \cdots$, where repeated indices suggest summation, and $\varepsilon_4^G = 2\varepsilon_{23}^G$, etc. Si was modeled to order three in ε^G with c_{ij} and c_{ijk} values from ultrasound experiments [17]. SiO_2 was modeled to order four in ε^G with c_{ij}, c_{ijk}, and c_{ijkl} values from ultrasound and shock-loading data [18, 19]; these constants were used to simulate nanopillar compression with good experimental agreement [20]. The full set of c_{ijkl} values were generated from the published constants using rotational symmetry. Plastic deformation in the SiO_2 was neglected due to the compressive stress not exceeding the compressive yield stress of −6.8 GPa (calculated via [20]) and plasticity not being observed in tension [20, 21].

3. Results and discussion

Figure 1 shows representative SEM, TEM, and STEM images of native SiNWs ($t = 0$ min) produced via the VLS growth

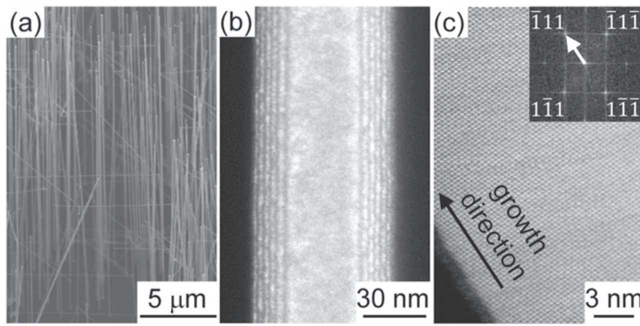

Figure 1. (a) SEM, (b) TEM, and (c) STEM images of native SiNWs. The native SiNWs were 25 to 30 μm in length, with a near-hexagonal cross-section and a defect-free lattice. The $\langle 111 \rangle$ growth direction was confirmed by the 0.32 nm lattice spacing and a Fourier transform of the STEM image.

process. From figure 1(a), SiNW lengths were found to be 25 to 30 μm for the prescribed growth conditions; these lengths were large enough to ensure adhesion between the end of a SiNW fixed to the Si(100) substrate during bending tests, but small enough to minimize changes in the cross-sectional area during VLS growth. Typical native SiNW cross-sections were near-hexagonal in shape as revealed by the fringes [22] in the TEM image (diffraction vector $\boldsymbol{g} = \langle 111 \rangle$) in figure 1(b), with nearly-flat $\{112\}$ facets as depicted elsewhere [23]. Additional high-resolution STEM images indicated a defect-free lattice (figure 1(c)) and a $\langle 111 \rangle$ growth direction, the latter of which was confirmed by the 0.32 nm lattice spacing and Fourier transforms of the STEM images (figure 1(c) inset). Furthermore, R_{NW} and t_{ox} for the native SiNWs were 30.6 nm $\pm$ 2.4 nm and 1.8 nm $\pm$ 0.2 nm, respectively. As such, $2R_{NW}$ and t_{ox} are in good agreement with the diameters of the Au nanoparticles used for VLS growth and reported values for native SiO_2 on SiNWs [24], respectively. On oxidation, R_{NW} and t_{ox} increased at small t, but converged to steady-state values at large t, as shown in the images in figures 2(a)–(f) and the resulting values for R_{NW} and t_{ox} in figure 2(g). At small t, the increases in R_{NW} and t_{ox} can be explained by assuming 1 mol of Si is transformed into 1 mol of SiO_2, and noting the greater molar volume of SiO_2 relative to Si [25]. It is also important to comment on the convergence of R_{NW} and t_{ox} at large t: previous studies on the oxidation of SiNWs also revealed this so-called self-limiting oxidation, and demonstrated that the final values for t_{ox} were dependent on R_{NW} and t [26]. Two main theories have been developed to explain the decrease in oxidation rate at large t. In the first theory, the oxidation is diffusion-limited, due to an increase in the activation energy for diffusion to the Si/SiO_2 interface [27]. In the second theory, oxidation is reaction-limited, and based on a decrease in the reaction rate at the Si/SiO_2 interface [28] as described by a two-dimensional non-planar model for Si [29]. Interestingly, both theories cite the radial compressive stress at the Si/SiO_2 interface for the self-limiting behavior. Regardless of the mechanism, it is clear from figure 2 that the steady-state R_{NW} and t_{ox} values for these particular SiNWs were reached at t of $\approx$7 min and 30 min, respectively.

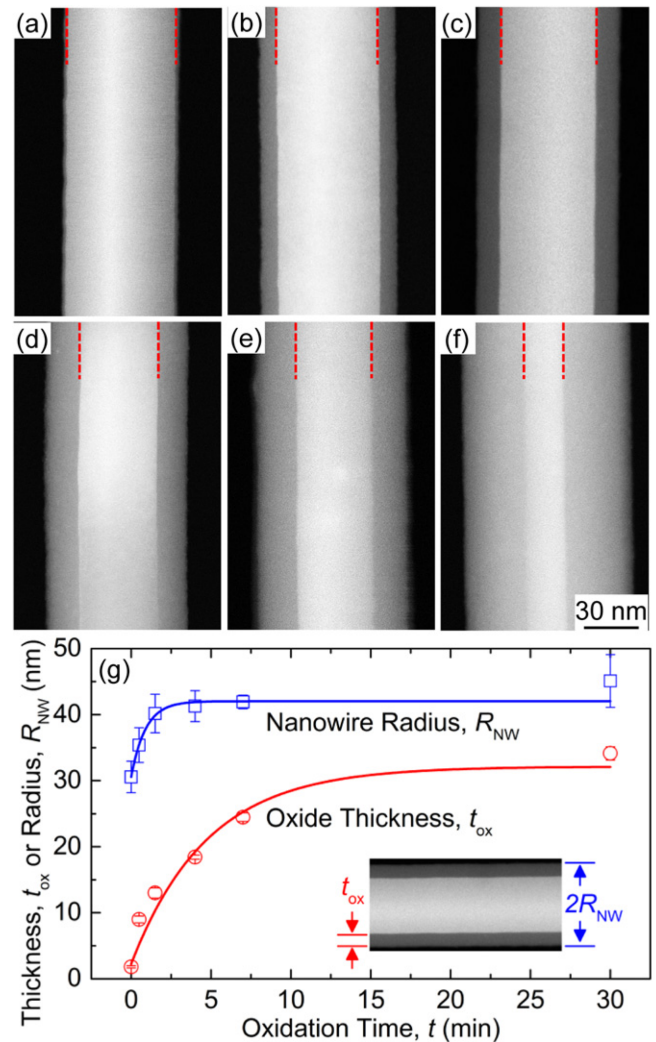

Figure 2. STEM images of SiNWs subjected to rapid thermal oxidation at 1000 °C for times t of (a) 0 min, (b) 0.5 min, (c) 1.5 min, (d) 4 min, (e) 7 min, and (f) 30 min. The STEM images shown in (a)–(f) are randomly sampled from the examined SiNWs, and do not denote the same SiNW at different t. (g) On oxidation, R_{NW} and t_{ox} increased at small t, but converged to their final values at large t. The self-limiting oxidation was likely due to large radial compressive stress at the Si/SiO_2 interface. Mean values and standard deviations are based on at least 10 measurements. Solid lines are a guide to the eyes.

The fracture properties of the SiNWs were measured by AFM bending tests for all t. The AFM topography images of bent SiNWs just prior to fracture are shown in figures 3(a)–(f). In most cases, the SiNW fractured *after* the next manipulation step, as confirmed by the subsequent topography image. On occasion, the SiNW fractured *during* a given image, as shown in figure 3(e). The scan direction for the image was bottom to top, and hence captured the profiles of the bent SiNW just prior to fracture followed by the broken SiNW end just after fracture. In both cases, the longer end of the broken SiNW returned to its near-original position and exhibited no signs of permanent deformation, implying that failure was due to brittle fracture. The calculated values for the local κ in the bent SiNWs are superimposed on the AFM

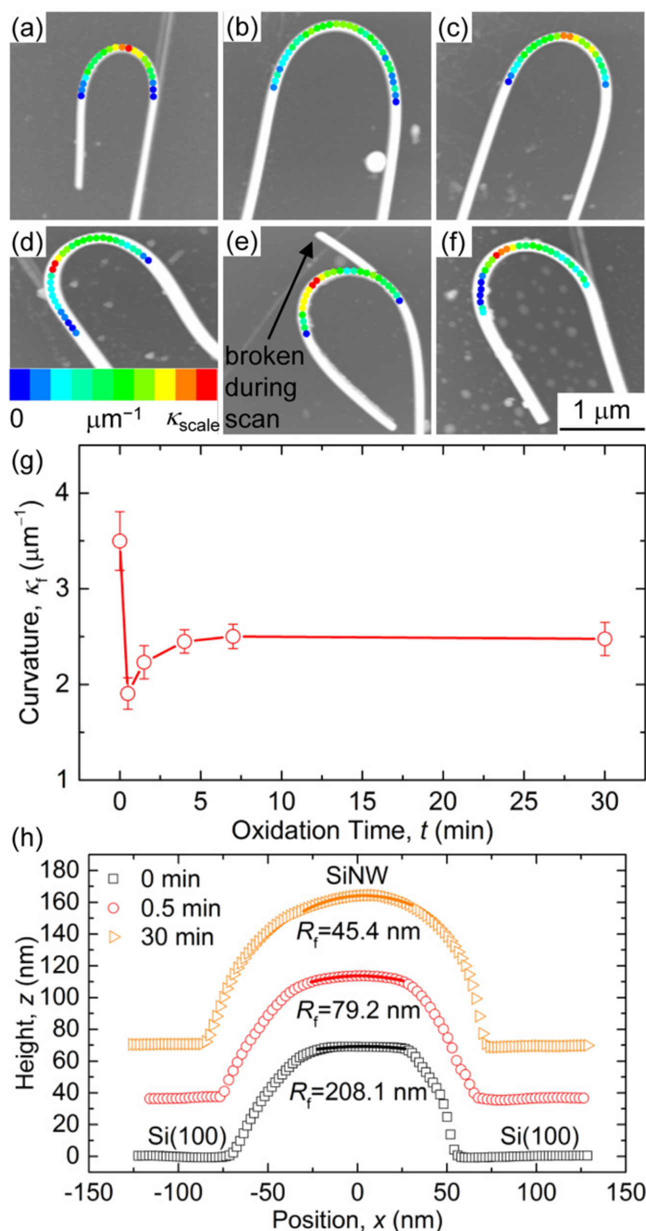

Figure 3. AFM topography images of SiNWs just prior to fracture for times t of (a) 0 min, (b) 0.5 min, (c) 1.5 min, (d) 4 min, (e) 7 min, and (f) 30 min. The images are taken with different tips and at random points in the tip wear process, and therefore do not exhibit the observed increase in R_{NW} with t (figure 2), due to varying degrees of tip convolution. The local values for κ are shown at 100 nm increments, where κ_{scale} is 3.5 μm^{-1} for (a) and 2.5 μm^{-1} for (b)–(f). (g) AFM curvature at fracture as a function of t. κ_f decreased non-monotonically as t increased. Mean values and standard deviations are based on at least 10 measurements. Solid line is a guide to the eyes. (h) AFM cross-sectional profiles at various t. At small t, R_f was large and the facet edges were distinct, while at large t, R_f approached R_{NW} and the facet edges were smooth.

profiles in figures 3(a)–(f); the κ measurements were equally spaced at 100 nm increments over the lengths of the SiNWs. κ_f was taken to be the maximum κ in each SiNW. In general, κ_f was located in the middle of the SiNW loop and corresponded well with the SiNW fracture location, both of which are particularly apparent in figure 3(e). Moreover, the values for κ_f at a given t were found to be independent of when the fracture event occurred (e.g., after a manipulation step or during an image) and therefore not dictated by the sizes of the manipulation displacements. In general, it is evident that κ_f decreased with t, as shown qualitatively in figures 3(a)–(f) and quantitatively in the average κ_f values in figure 3(g). However, the decrease in κ_f with t was non-monotonic. Instead, κ_f decreased from 3.5 to 1.9 μm^{-1} at small t, but gradually recovered back to 2.5 μm^{-1} at large t.

Figure 3(h) shows cross-sectional profiles of the SiNWs at different t, as measured by AFM. Measured profiles were a convolution of the true SiNW cross-section and the AFM tip shape and hence the measured facet radii R_{meas} are a convolution of the actual facet radii R_f and the AFM tip radius R_t. Assuming additive convolution ($R_{meas} = R_f + R_t$) and an average value of $R_t \approx 20$ nm, R_f was calculated from the measured profiles. Overall, R_f decreased as t increased. At small t, R_f was large and the facet edges were pronounced, which are indicative of a near-hexagonal cross-section. At large t, R_f approached R_{NW} and the facet edges were smooth, which point to a near-circular cross-section. This oxidation-induced shape change is consistent with other work on microscale Si features [30] and SiNWs [31]. To capture these changes in the FEA models, it was essential to re-create the cross-sections as a function of t, based on the STEM data in figure 2(g). The exteriors of the cross sections were attained by a linear interpolation between an assumed as-fabricated SiNW of perfect hexagonal section and the $t = 30$ min SiNWs of perfect cylindrical section. The interiors of the cross-sections, or the Si/SiO_2 interface, were defined by radial scaling of the exterior cross-sections from the STEM data. The facet radii were calculated from the interpolated STEM data for comparison with the AFM data in figure 3(h). The generated cross-sectional profiles are shown in figures 4(a)–(f). Qualitatively, the profiles are in agreement with observed trends, with the cross-section varying from nearly-hexagonal to fully-circular. Quantitatively, the generated R_f and R_{NW} are well-aligned with the data, as validated by the small deviations from the trend line in figure 4(g). In all, it is clear that the interpolation scheme presented herein accurately depicts the oxidation kinematics.

Figure 5(a) shows σ_{max} in the Si and SiO_2 for $t = 0$ min and $t = 30$ min as a function of κ, as revealed from FEA. Linear and nonlinear FEA are presented, the latter taking into account both the material and geometrical nonlinear behavior of the highly deformed SiNWs apparent in figures 3(a)–(f). The vertical arrows in figure 5(a) indicate the κ_f values for the two oxidation states from figure 3(g). The σ_{max} values from the linear FEA can be compared to previous SiNW σ_f measurements by noting that $\sigma_f = \sigma_{max}$ at $\kappa = \kappa_f$: for $t = 0$ min, $\sigma_{max} = 18.9$ GPa in the Si, which compares to $\sigma_f = 18$ GPa as reported earlier [6]; for $t = 30$ min, $\sigma_{max} = 8.1$ GPa in the SiO_2, which compares to $\sigma_f = 6.2$ GPa as reported earlier [13]. Therefore, linear deformation interpretations of σ_{max} at $t = 0$ min and $t = 30$ min are in agreement with earlier σ_f based on similar linear-elastic interpretations. However, the large κ_f suggest that σ_f are more appropriately determined from a nonlinear analysis.

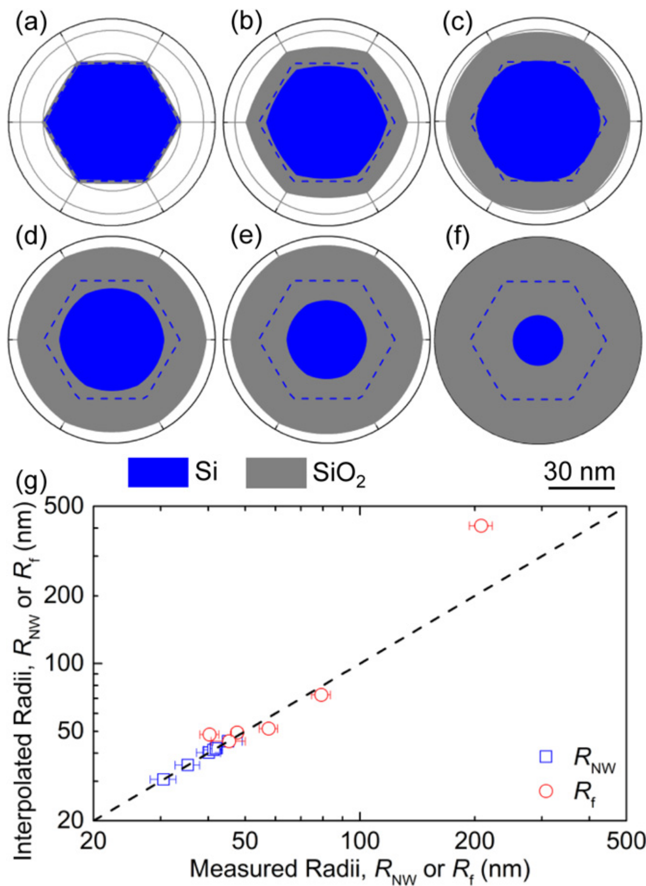

Figure 4. The interpolated SiNW profiles for times t of (a) 0 min, (b) 0.5 min, (c) 1.5 min, (d) 4 min, (e) 7 min, and (f) 30 min. The profile for the theoretical as-fabricated SiNW of perfect hexagonal section is depicted by the dashed blue line. (g) Qualitatively, the profiles are in accordance with the observed trends, with the cross-section changing from nearly-hexagonal to fully-circular with t. The generated values for R_f and R_{NW} are also well-aligned with the data, as validated by small deviations from the unity trend line. Mean values and standard deviations are based on at least 10 measurements.

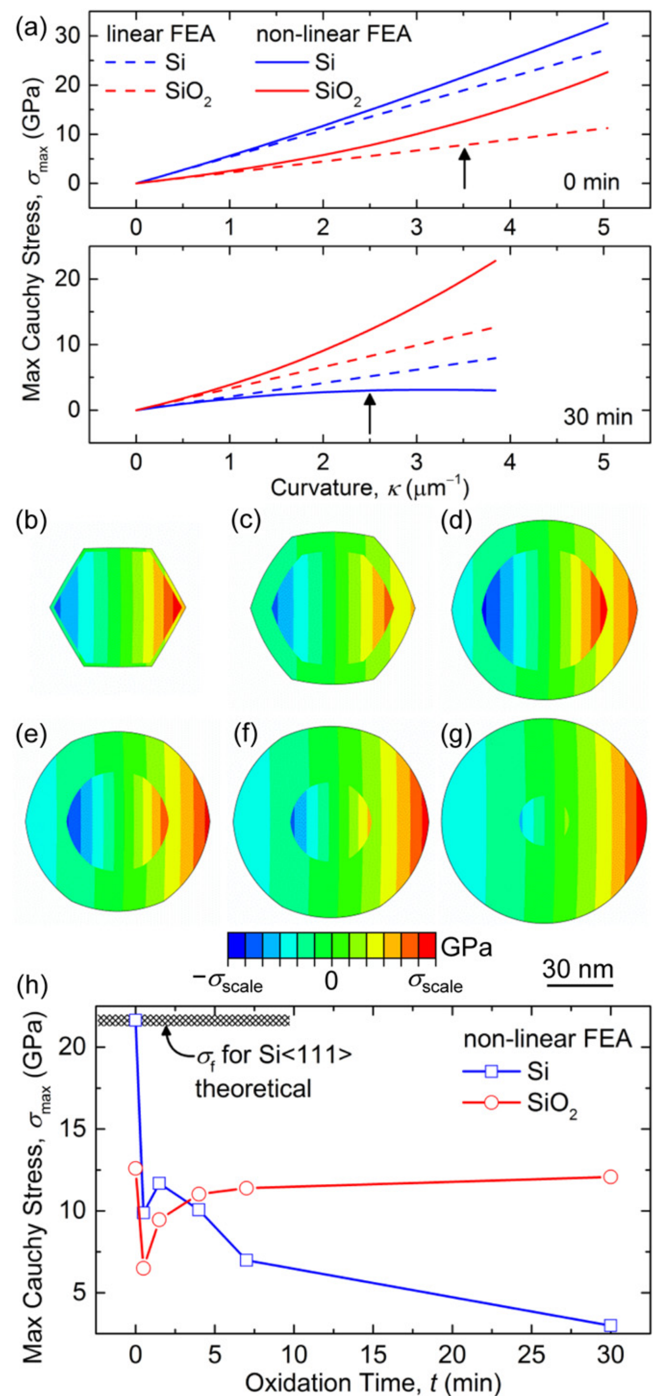

Figure 5. (a) Maximum longitudinal Cauchy stress σ_{max} in the Si and SiO_2 for $t = 0$ min and $t = 30$ min as a function of κ. Linear and nonlinear FEA calculations are presented, the latter taking into account both material and geometrical nonlinear behavior of the highly deformed SiNWs. Stress contour maps for times t of (b) 0 min, (c) 0.5 min, (d) 1.5 min, (e) 4 min, (f) 7 min, and (g) 30 min, calculated with the full nonlinear FEA at the measured κ_f. σ_{scale} is 21.6 GPa for (b) and 12.1 GPa for (c)–(g). (h) σ_{max} in Si and SiO_2 as a function of t from the full nonlinear FEA. Mean values are based on at least 10 measurements. Solid lines are a guide to the eyes.

Figures 5(b)–(g) show contours of stress in the SiNWs calculated using a full nonlinear analysis at the measured κ_f. On initial oxidation, σ_{max} appears in the Si. As oxidation proceeds, however, the stress in the Si diminishes considerably, and σ_{max} moves to the SiO_2. To interpret the shifting contours, σ_{max} values need to be compared to the sustainable stresses of the materials. Figure 5(h) shows σ_{max} in the Si and SiO_2 as a function of t. For the native SiNWs, σ_{max} in the Si is comparable to the theoretical strength of Si $\langle 111 \rangle$, ≈22 GPa, shown by the shaded band. However, σ_{max} in the SiO_2, ≈12 GPa, is considerably greater than the SiO_2 theoretical strength of $E/10 \approx 7$ GPa, where E is Young's modulus. Hence, it is ambiguous whether failure initiated in the Si or SiO_2 for the native SiNWs. In either case, these stress, and hence strength, values are some of the largest reported for both materials, and are clearly in the realm of theoretical strengths controlled by either inter-atomic bond breaking [32] (if the SiNWs are defect-free, as suggested in figure 1(c)) or atomic-scale defects [33] (if the SiNWs have defects not detected in the STEM). On initial oxidation, σ_{max} in the Si and SiO_2 decrease substantially. However, the stress in the Si was reduced significantly relative to the theoretical strength of Si, whereas the stress in the SiO_2 remained comparable to theoretical strength of SiO_2. The implication is

that failure is now initiated in the oxide, likely from surface roughness at the SiNW exterior on the newly-formed SiO_2 surface. Continued oxidation led to almost monotonic decrease in σ_{max} in the Si at failure and gradual increase in σ_{max} in the SiO_2. The increase in σ_{max} in the SiO_2 suggests a related reduction in the potency of the strength-limiting defects, perhaps from a smoothing of the SiO_2. The overall decrease in σ_f is in good agreement with recent molecular dynamic simulations of the fracture of Si with surface steps; in that study, σ_f decreased from 23 to 14 GPa as the number of surface steps increased from 1 to 6 [34]. The authors suggested that the decrease in σ_f is due to a transient process, in which the roughness initially increases on SiO_2 nucleation but then decreases with complete SiO_2 formation [35].

Altogether, the data presented herein and elsewhere [34, 36] suggest that the σ_f versus t trend for Si is dependent on the length scales of the component and the strength-limiting flaw sizes, a hypothesis originally presented in a recent review paper [8]. For nanoscale components with native σ_f close to the theoretical limit (≈22 GPa) that are defect-free or with atomic-scale defects, it was shown here that σ_f decreased at small t and only *partially* recovered at large t, indicating that the oxidation process led to an irreversible roughening of the Si surface. For nanoscale components with moderate native σ_f (≈9 to 13 GPa) and critical flaw sizes on the order of a few to tens of nm, a recent report showed that σ_f decreased at small t and then *fully* recovered at large t, signifying that the roughness of the oxidized Si surface was close to that of the native Si surface (i.e., the initial oxidation-induced roughening of the Si surface was reversible) [34]. For microscale components with relatively small native σ_f (≈1 to 5 GPa) and critical flaw sizes on the order of tens to hundreds of nm, another study showed that σ_f increased with oxidation, presumably due to the formation of oxygen bridges between the critical flaws induced from the fabrication process [36].

4. Conclusions

In conclusion, the strength of SiNWs has been measured as a function of oxidation state. On initial oxidation, the very thin oxide layer on the near-hexagonal native SiNWs extended outward and inwards, leading to an increase in both R_{NW} and t_{ox} and a transformation to a circular section. SiNW strengths were calculated from nonlinear FEA simulations and AFM-based measurements of κ_f. For native SiNWs, σ_{max} in the Si was comparable to the theoretical strength of Si$\langle 111 \rangle$, ≈22 GPa. In the oxidized SiNWs, σ_{max} in the Si was much less than this value, but σ_{max} in the SiO_2 was comparable to the theoretical strength of SiO_2, ≈6 to 12 GPa. The measurements point to a change in the failure mechanism between native SiNWs, in which fracture originated via inter-atomic bond breaking or atomic-scale defects in the Si, and oxidized SiNWs, in which fracture is initiated from roughness or nanoscale defects in the SiO_2. In all, the σ_{max}, and hence σ_f, values are approximately equal to the theoretical strengths for both Si and SiO_2, and an order of magnitude greater than those for microscale Si [37–39] and SiO_2 [40, 41] components.

Acknowledgments

Specific commercial equipment, instruments, and materials that are identified in this report are listed in order to adequately describe the experimental procedure and are not intended to imply endorsement or recommendation by the National Institute of Standards and Technology (NIST). Contribution of NIST, an agency of the US government; not subject to copyright. Unless otherwise noted, experimental uncertainties are one standard deviation of the mean.

References

[1] Feng X L, He R, Yang P and Roukes M L 2007 Very high frequency silicon nanowire electromechanical resonators *Nano Lett.* **7** 1953–9
[2] Cui Y, Wei Q, Park H and Lieber C M 2001 Nanowire nanosensors for highly sensitive and selective detection of biological and chemical species *Science* **293** 1289–92
[3] Huang Y, Duan X and Lieber C M 2005 Nanowires for integrated multicolor nanophotonics *Small* **1** 142–7
[4] He R and Yang P 2006 Giant piezoresistance effect in silicon nanowires *Nat. Nanotechnol.* **1** 42–6
[5] Boukai A I, Bunimovich Y, Tahir-Kheli J, Yu J-K, Goddard W A III and Heath J R 2008 Silicon nanowires as efficient thermoelectric materials *Nature* **451** 168–71
[6] Stan G, Krylyuk S, Davydov A V, Levin I and Cook R F 2012 Ultimate bending strength of Si nanowires *Nano Lett.* **12** 2599–604
[7] Dubois S-M, Rignanese G-M, Pardoen T and Charlier J-C 2006 Ideal strength of silicon: an ab initio study *Phys. Rev.* B **74** 235203
[8] DelRio F W, Cook R F and Boyce B L 2015 Fracture strength of micro- and nano-scale silicon components *Appl. Phys. Rev.* **2** 021303
[9] Hoffmann S, Utke I, Moser B, Michler J, Christiansen S H, Schmidt V, Senz S, Werner P, Gosele U and Ballif C 2006 Measurement of the bending strength of vapor−liquid−solid grown silicon nanowires *Nano Lett.* **6** 622–5
[10] Zhu Y, Xu F, Qin Q, Fung W Y and Lu W 2009 Mechanical properties of vapor−liquid−solid synthesized silicon nanowires *Nano Lett.* **9** 3934–9
[11] Tang D-M, Ren C-L, Wang M-S, Wei X, Kawamoto N, Liu C, Bando Y, Mitome M, Fukata N and Golberg D 2012 Mechanical properties of Si nanowires as revealed by in situ transmission electron microscopy and molecular dynamics simulations *Nano Lett.* **12** 1898–904
[12] Weibull W 1951 A statistical distribution function of wide applicability *J. Appl. Mech. Trans. ASME* **18** 293–7
[13] Stan G, Krylyuk S, Davydov A V and Cook R F 2012 Bending manipulation and measurements of fracture strength of silicon and oxidized silicon nanowires by atomic force microscopy *J. Mater. Res.* **27** 562–70
[14] Krylyuk S, Davydov A V, Levin I, Motayed A and Vaudin M D 2009 Rapid thermal oxidation of silicon nanowires *Appl. Phys. Lett.* **94** 063113
[15] Tummers B DataThief III, 2006 http://datathief.org/
[16] Dassault Systems SIMULIA Corp. 2011 *ABAQUS, v. 6.14-5* (Johnston, RI: Dassault Systems SIMULIA Corp.)
[17] McSkimin H J and Andreatch P 1964 Measurement of third-order moduli of silicon and germanium *J. Appl. Phys.* **35** 3312–9
[18] Bogardus E H 1965 Third-order elastic constants of Ge, MgO, and fused SiO_2 *J. Appl. Phys.* **36** 2504–13

[19] Kondo K, Iio S and Sawaoka A 1981 Nonlinear pressure dependence of the elastic moduli of fused quartz up to 3 GPa *J. Appl. Phys.* **52** 2826–31

[20] Lacroix R, Chomienne V, Kermouche G, Teisseire J, Barthel E and Queste S 2012 Micropillar testing of amorphous silica *Int. J. Appl. Glass Sci.* **3** 36–43

[21] Kermouche G, Barthel E, Vandembroucq D and Dubujet P 2008 Mechanical modelling of indentation-induced densification in amorphous silica *Acta Mater.* **56** 3222–8

[22] Williams D B and Carter C B 1996 *Transmission Electron Microscopy: A Textbook for Materials Science* (New York: Plenum)

[23] Oleshko V P, Williams E H, Davydov A V, Krylyuk S, Motayed A, Ruzmetov D, Lam T, Lezec H J and Talin A A 2013 Analytical electron microscopy of semiconductor nanowire functional materials and devices for energy applications *J. Phys.: Conf. Ser.* **471** 012017

[24] Gordon M J, Baron T, Dhalluin F, Gentile P and Ferret P 2009 Size effects in mechanical deformation and fracture of cantilevered silicon nanowires *Nano Lett.* **9** 525–9

[25] Kedzierski J, Bokor J and Kisielowski C 1997 Fabrication of planar silicon nanowires on silicon-on-insulator using stress limited oxidation *J. Vac. Sci. Technol.* B **15** 2825–8

[26] Liu H I, Biegelsen D K, Johnson N M, Ponce F A and Pease R F W 1993 Self-limiting oxidation of Si nanowires *J. Vac. Sci. Technol.* B **11** 2532–7

[27] Liu H I, Biegelsen D K, Ponce F A, Johnson N M and Pease R F W 1994 Self-limiting oxidation for fabricating sub-5 nm silicon nanowires *Appl. Phys. Lett.* **64** 1383–5

[28] Heidemeyer H, Single C, Zhou F, Prins F E, Kern D P and Plies E 2000 Self-limiting and pattern dependent oxidation of silicon dots fabricated on silicon-on-insulator material *J. Appl. Phys.* **87** 4580–5

[29] Kao D-B, McVittie J P, Nix W D and Saraswat K C 1988 Two-dimensional thermal oxidation of silicon: II. Modeling stress effects in wet oxides *IEEE Trans. Electron Devices* **ED-35** 25–37

[30] Marcus R B and Shang T T 1982 The oxidation of shaped silicon surfaces *J. Electrochem. Soc.* **129** 1278–82

[31] Kawashima T, Saitoh T, Komori K and Fujii M 2009 Synthesis of Si nanowires with a thermally oxidized shell and effects of the shell on transistor characteristics *Thin Solid Films* **517** 4520–6

[32] Kelly A 1973 *Strong Solids* (Oxford: Clarendon)

[33] Zhou G W, Zhang Z, Bai Z G, Feng S Q and Yu D A 1998 Transmission electron microscopy study of Si nanowires *Appl. Phys. Lett.* **73** 677–9

[34] Grutzik S J, Milosevic E, Boyce B L and Zehnder A T 2015 Oxide driven strength evolution of silicon surfaces *J. Appl. Phys.* **118** 195304

[35] Neuwald U, Hessel H E, Feltz A, Memmert U and Behm R J 1992 Initial stages of native oxide growth on hydrogen passivated Si(111) surfaces studied by scanning tunneling microscopy *Appl. Phys. Lett.* **60** 1307–9

[36] Ericson F and Schweitz J-A 1990 Micromechanical fracture strength of silicon *J. Appl. Phys.* **68** 5840–4

[37] Gaither M S, DelRio F W, Gates R S, Fuller E R and Cook R F 2010 Strength distribution of single-crystal silicon theta-like specimens *Scr. Mater.* **63** 422–5

[38] Gaither M S, DelRio F W, Gates R S and Cook R F 2011 Deformation and fracture of single-crystal silicon theta-like specimens *J. Mater. Res.* **26** 2575–89

[39] Gaither M S, Gates R S, Kirkpatrick R, Cook R F and DelRio F W 2013 Etching process effects on surface structure, fracture strength, and reliability of single-crystal silicon theta-like specimens *J. Microelectromech. Syst.* **22** 589–602

[40] Sharpe W N Jr, Pulskamp J, Gianola D S, Eberl C, Polcawich R G and Thompson R J 2007 Strain measurements of silicon dioxide microspecimens by digital imaging processing *Exp. Mech.* **47** 649–58

[41] Chu J and Zhang D 2009 Mechanical characterization of thermal SiO_2 micro-beams through tensile testing *J. Micromech. Microeng.* **19** 095020